Monthly Notices
of the
ROYAL ASTRONOMICAL SOCIETY

MNRAS **505,** 3165–3176 (2021)
Advance Access publication 2021 May 29

https://doi.org/10.1093/mnras/stab1559

Constraining the solar neighbourhood age–metallicity relation from white dwarf–main sequence binaries

A. Rebassa-Mansergas,[1,2]★ J. Maldonado,[3] R. Raddi,[1] A. T. Knowles,[1] S. Torres,[1,2] M. Hoskin,[4] T. Cunningham,[4] M. Hollands,[4] J. Ren,[5] B. T. Gänsicke,[4] P.-E. Tremblay,[4] N. Castro-Rodríguez,[6,7,8] M. Camisassa[1,9] and D. Koester[10]

[1]*Departament de Física, Universitat Politècnica de Catalunya, c/Esteve Terrades 5, E-08860 Castelldefels, Spain*
[2]*Institute for Space Studies of Catalonia, c/Gran Capità 2–4, Edif. Nexus 104, E-08034 Barcelona, Spain*
[3]*INAF - Osservatorio Astronomico di Palermo, Piazza del Parlamento 1, I-90134 Palermo, Italy*
[4]*Department of Physics, University of Warwick, Coventry CV4 7AL, UK*
[5]*CAS Key Laboratory of Space Astronomy and Technology, National Astronomical Observatories, Chinese Academy of Sciences, Beijing 100101, China*
[6]*Instituto de Astrofísica de Canarias, E-38200 La Laguna, Tenerife, Spain*
[7]*Depart. de Astrofísica, Universidad de La Laguna, E-38206 La Laguna, Tenerife, Spain*
[8]*GRANTECAN, Cuesta de San José s/n, E-38712 Breña Baja, La Palma, Spain*
[9]*Department of Applied Mathematics, University of Colorado, Boulder, CO 80309-0526, USA*
[10]*Institut für Theoretische Physik und Astrophysik, Universitï Kiel, D-24098, Kiel, Germany*

Accepted 2021 May 26. Received 2021 May 26; in original form 2021 March 26

ABSTRACT

The age–metallicity relation (AMR) is a fundamental tool for constraining the chemical evolution of the Galactic disc. In this work, we analyse the observational properties of this relation using binary stars that have not interacted consisting of a white dwarf (WD) – from which we can derive the total age of the system – and a main sequence (MS) star – from which we can derive the metallicity as traced by the [Fe/H] abundances. Our sample consists of 46 widely separated, but unresolved spectroscopic binaries identified within the Sloan Digital Sky Survey, and 189 WD plus MS common proper motion pairs identified within the second data release of *Gaia*. This is currently the largest WD sample for which the metallicity of their progenitors have been determined. We find a flat AMR displaying a scatter of [Fe/H] abundances of approximately ±0.5 dex around the solar metallicity at all ages. This independently confirms the lack of correlation between age and metallicity in the solar neighbourhood that is found in previous studies focused on analysing single MS stars and open clusters.

Key words: techniques: spectroscopic – stars: abundances – binaries: spectroscopic – stars: low-mass – white dwarfs – solar neighbourhood..

1 INTRODUCTION

The formation and assembly history of our Galaxy can be traced through the chemical composition, age, position, and velocity of its constituent stars. In particular, the age–metallicity relation (AMR), which is the observed connection between the age and the chemical abundances of stars, can provide vital constraints on the formation and evolution of the Galactic disc. The AMR has therefore been widely studied during the last decades (e.g. see the reviews of Nomoto, Kobayashi & Tominaga 2013 and Feltzing & Chiba 2013 and the more recent studies by Bergemann et al. 2014 and Wojno et al. 2018). Some of the very early works on this topic found evidence for an AMR in which the oldest stars have the lowest metallicity (e.g Twarog 1980, Rocha-Pinto et al. 2000, Soubiran et al. 2008). This relation was found to behave as expected in a formation and evolution scenario in which stars form from the metal-enriched gas left by previous generations of stars. However, there have been evidence against an AMR existing at all, with large metallicity dispersions found in comprehensive or more recent works (e.g. Edvardsson et al. 1993; Haywood et al. 2013; Bergemann et al. 2014; Wu et al. 2021). The lack of correlation between age and metallicity in the Milky Way suggests a much more complicated formation scenario (Feuillet et al. 2019).

A major limitation of most previous studies is the measurement of stellar ages, which is a difficult task. Historically, the ages of stars were estimated through chromospheric activity levels (e.g. Barry 1988; Rocha-Pinto et al. 2000) or through isochrone fitting with an appropriate metallicity (e.g. Jørgensen & Lindegren 2005; Howes et al. 2019). More recently, the combination of spectroscopy and asteroseismology has been used to estimate stellar masses and to derive stellar ages (e.g. Casagrande et al. 2016; Pinsonneault et al. 2018).

An alternative method to estimate the age component of the AMR is to use white dwarfs (WDs) as cosmic clocks. WDs are the typical end stage of the vast majority of main sequence (MS) stars (see the review of Althaus et al. 2010), and because their evolution follows a relatively simple and well understood cooling process, they can be used as reliable observational measures of stellar age (e.g. Fouesneau et al. 2019; Lam et al. 2020; Qiu et al. 2020). In order to determine the total age of a WD, defined as the sum of its cooling age and its MS

★ E-mail: alberto.rebassa@upc.edu

progenitor lifetime, two processes are required. First, a prescription for evolutionary cooling sequences provides a measure of the WD cooling age from observed determinations of effective temperature ($T_{\rm eff}$) and surface gravity (log g). To that end, we adopt the widely used sequences of the La Plata group (e.g. Renedo et al. 2010; Althaus et al. 2015; Camisassa et al. 2016, 2019), which encompass the full range of WD masses and the most updated prescriptions in the treatment of physical processes. Secondly, a relationship between the mass of the WD and the mass of its progenitor is required to obtain a MS lifetime estimate. This initial-to-final mass relation (e.g. Catalán et al. 2008; Cummings et al. 2018; Barrientos & Chanamé 2021) enables the estimation of MS star masses from measures of the current day WD masses, which in turn, can be used to determine the time spent on the MS from evolutionary sequences, provided the metallicity is known. Once we know the MS lifetimes and the cooling times, the total ages are determined as the sum of these two ages.

Because a significant fraction of known MS stars in our Galaxy are expected to be in multiple systems, particularly binaries (e.g. Yuan et al. 2015), and because the majority of MS stars end their lives as WDs, it follows that there exists a large number of binary systems consisting of a primary (more massive) star that has evolved to a WD, and a secondary MS star. The majority of these WD–MS binary systems are expected to have orbital separations that are wide enough to avoid mass transfer episodes, thus allowing one to treat them as if they were isolated (Willems & Kolb 2004). These wide WD–MS binary systems can therefore be considered as useful probes in the study of the Galactic AMR. An accurate age of the WD can be estimated via the process described above and the MS star metallicity can be measured via detailed spectroscopic matching to stellar models (e.g Bensby, Feltzing & Oey 2014; Holtzman et al. 2015). Assuming the two stars within the binary are coeval, a measurement of the WD age also gives an age estimate for the MS star, and thus the AMR can be probed using these systems. This work follows on from the initial study of Rebassa-Mansergas et al. (2016b), in which an AMR was determined from a pilot sample of 23 wide WD–MS binary systems identified within the Sloan Digital Sky Survey (SDSS; York et al. 2000; Eisenstein et al. 2011). Here, we continue this observational campaign and considerably enlarge the sample using WD–MS binaries in resolved common proper motion pairs (CPMPs) identified thanks to the *Gaia* mission (Gaia Collaboration 2016).

The structure for this paper is as follows. Section 2 presents the WD–MS binary samples used for this work. Section 3 describes the observations of both WDs and MS stars. Section 4 presents the results, which are discussed in Section 5. Finally, Section 6 presents our conclusions.

2 THE WD–MS BINARY SAMPLES

In this work, we use two different WD–MS binary samples to constrain the AMR.

The first is the catalogue of more than 3000 WD–MS binaries from the SDSS (Rebassa-Mansergas et al. 2016a). In particular, for this project, we select binaries containing a hydrogen-rich WD primary that display no significant radial velocity variations over a baseline of at least 2 d and have SDSS g magnitudes <19 mag. The first requirement ensures the binaries are widely separated and therefore very likely did not evolve through any phase of mass transfer (note that the orbital period distribution of close SDSS WD–MS binaries peaks at $\simeq$8 h and that there are very few close binaries with periods longer than 1 d, see Nebot Gómez-Morán et al. 2011). The second condition selects systems that are bright enough to allow for the derivation of reliable WD ages and MS star metallicities from spectroscopic observations at ground-based telescopes of medium and large apertures. In Rebassa-Mansergas et al. (2016b), we presented a pilot study of the AMR from 23 SDSS WD–MS binaries and here we extend the analysis to 29 additional systems.

We build our second WD–MS binary sample by mining the data release 2 of *Gaia* (Gaia Collaboration 2016, 2018a). Our approach here is to identify CPMPs that contain a WD and a MS star. This has two clear advantages over the SDSS WD–MS binary sample introduced in the previous paragraph. First, the WD and MS stars are separated enough to allow for independent observations of the two stellar components. This avoids any possible selection effects against the identification of binaries containing cool WDs, which are generally outshined by the MS companions in the SDSS sample (Rebassa-Mansergas et al. 2016a). These WDs are of great interest since they have the longest cooling ages and can hence be used to test the AMR at the intermediate/old ages. Secondly, the MS companions are not only M dwarfs, which are the dominant spectral types in the SDSS WD–MS binary sample, but also F-, G-, and K-type stars. M-dwarf metallicity calibrators that are based on the spectral analysis have been often criticized. For example, Lindgren & Heiter (2017) argue that, for individual M stars, different metallicity calibrations yield [Fe/H][1] abundances that differ by as much as 0.6 dex. The *Gaia* WD–MS binary sample containing F, G, and K companions allows us to avoid this possible issue, since it has been shown that metallicity calibrations provide similar values of [Fe/H] for such stars (e.g. Teixeira et al. 2016).

We searched for CPMP companions to the WDs that were identified by Gentile Fusillo et al. (2019) in *Gaia* DR2. From their catalogue, we selected 103 002 candidates with a probability of being a WD larger than 50 percent and a parallax uncertainty of better than 10 percent. Thus, we mined the *Gaia* DR2 archive searching for common proper motion MS companions within 100 000 au from the WD candidates. Our procedure mimics that of El-Badry & Rix (2018), although we used an input WD list and we adopted a wider search radius. By assuming the two stars are on a bound Keplerian orbit (cf. Andrews, Chanamé & Agüeros 2017; El-Badry & Rix 2018; Jiménez-Esteban, Solano & Rodrigo 2019), we impose an upper limit of 8.5 $M_{\odot}$ for the total mass of the system, which implies a maximum difference in projected velocities of $\Delta V_{\perp}$ (km s^{-1}) $\leq 2.73 \times (a/10^3 \text{ au})^{-1/2}$, where a is the projected separation in astronomical units. We applied standard astrometric and photometric cuts (Gaia Collaboration et al. 2018b; Lindegren 2018) to ensure that companions with good quality data are found. Hence, we identify 4415 WD–MS systems with distances $\lesssim$500 pc, with a lognormal distribution centred at $\log(1/\varpi) = 2.17 \pm 0.25$, where 0.25 is the standard deviation and ϖ is the measured parallax. A comparison with the catalogue of El-Badry & Rix (2018) shows that our search resulted in $\approx$1800 additional systems, while our catalogue does not contain 194 systems found by these authors. These differences are mostly explained by the use of an input WD list, which enables us to expand our catalogue towards larger distances from the Sun. A comparison with the most recent catalogue of CPMPs identified by El-Badry, Rix & Heintz (2021) confirms a 92 percent overlap, with the majority of pairs having a low probability of chance alignment as defined by the authors. The Hertzsprung–Russell diagram of our resolved CPMP candidates is shown in Fig. 1.

[1][Fe/H]$= \log\left(\frac{\rm nFe}{\rm nH}\right)_{*} - \log\left(\frac{\rm nFe}{\rm nH}\right)_{\odot}$, where $\left(\frac{\rm nFe}{\rm nH}\right)$ is the number abundance ratio of Fe relative to H for a given star ($*$) or for the Sun ($\odot$).

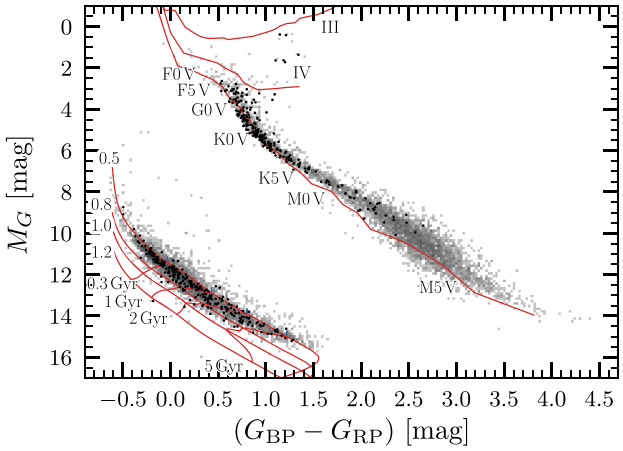

Figure 1. Hertzsprung–Russell diagram of *Gaia*-selected WD–MS common proper-motion pairs. The dwarf (V), sub-giant (IV), and giant (III) tracks are obtained from the Pickles (1998) spectral library. The cooling sequences for hydrogen-rich WDs of 0.5, 0.8, 1.0, and 1.2 $M_\odot$ are described by Camisassa et al. (2016, 2019). The isochrones for total WD ages, which is the pre-WD evolutionary time and the WD cooling age, are also shown for 0.3, 1, 2, and 5 Gyr. The black dots represent the companion stars with available [Fe/H] abundances from our spectroscopic follow-up and their WD primaries.

Table 1. Log of the observations including the telescope name, the observing mode (service, sm, or visitor, vm), the month dates, or period of the observations, the instrument used, and the number of taken spectra.

Telescope	Mode	Dates or period	Instrument	#spec
VLT	sm	P101	X-Shooter	17
GTC	sm	2016B, 2017A	OSIRIS	10
GTC	sm	2017B, 2018A	EMIR	12
WHT	vm	Oct. 2018, Feb. & Apr. 2019	ISIS	122
INT	vm	Jul. 2019	IDS	92
TNG	sm	2018B	HARPS-N	106
Mercator	vm	Dec. 2018 & Jan. 2019	HERMES	377
Xinglong2.16	vm	Dec. 2018, Feb. 2019 & June 2020	echelle	51

3 OBSERVATIONS OF THE WD–MS BINARY SAMPLE

We adopted different strategies to observe the WD–MS binaries belonging to the two samples described in the previous section. A log of the observations is shown in Table 1.

SDSS WD–MS binaries are unresolved despite the fact that they display no radial velocity variations. This is because they are generally located at far enough distances (≃400–500 pc; Rebassa-Mansergas et al. 2010). Therefore, one single spectrum collects the dispersed light from both components.

The *Gaia* WD–MS binaries we selected in this work are members of spatially resolved CPMPs. As a consequence, we aimed at obtaining one optical spectrum for each component.

3.1 SDSS WD–MS binaries

3.1.1 Very Large Telescope

We observed 17 SDSS WD–MS binaries with the *Very Large Telescope* (*VLT*), at Cerro Paranal (Chile), and the X-Shooter instrument (Vernet et al. 2011). X-Shooter provides spectra in three arms simultaneously covering a wavelength range of ≃3000–25 000 Å (UVB arm; 3000–5600 Å, VIS arm; 5500–10 200 Å, NIR arm; 10 200–24 800 Å). The observations were performed in service mode using the 0.9–1 arcsec slits, which resulted in spectra with resolving power 4350/7450/5300 in the UVB/VIS/NIR arms, respectively. We reduced and calibrated the data using the ESOREFLEX X-Shooter pipeline, version 3.3.5.

3.1.2 Gran Telescopio Canarias

We obtained service mode optical and near-infrared spectra with the Gran Telescopio Canarias (GTC), for 10 and 12 additional SDSS WD–MS binaries using the OSIRIS and EMIR instruments, respectively. We used the 2000B and 2,500R gratings together with the 0.6 arcsec slit width for the optical OSIRIS observations, which resulted in optical spectra covering the 3960–5690 Å and 5590–7680 Å wavelength ranges at resolving powers of 2000 and 2500. The EMIR observations were performed using the K grism and the 0.8 arcsec slit width, thus providing spectra covering the 20 300–23 850 Å wavelength range at a resolving power of 3100. The OSIRIS spectra were reduced using the PAMELA software (Marsh 1989) and calibrated using MOLLY.[2] The EMIR spectra were reduced and calibrated using REDEMIR, a new GTC pipeline written in PYTHON. In a first step, it eliminates the contribution of the sky background using consecutive A–B pairs. Subsequently, the spectra are flat-fielded, calibrated in wavelength, and combined to obtain the final spectrum in the K band.

3.2 *Gaia* WD–MS CPMPs

3.2.1 William Herschel Telescope

Low-resolution spectra for 122 WDs were obtained at the 4.2-metre *William Herschel Telescope* (*WHT*) at El Roque de los Muchachos observatory in La Palma in visitor mode during 2018 and 2019. We used the ISIS (Intermediate-dispersion Spectrograph and Imaging System) instrument and the 1 arcsec width long-slit together with two different gratings, the 600 B and 600 R. This provided blue- and red-arm simultaneous spectra at a resolving power of 600, respectively covering the ≃3600–5100 Å and ≃5600–7200 Å wavelength ranges. Arc spectra were taken along the nights to account the flexure of the instrument. The *WHT* spectra were reduced and calibrated using the PAMELA and MOLLY softwares, respectively.

3.2.2 Isaac Newton Telescope

Low-resolution spectra of 92 additional WDs were obtained at the *Isaac Newton Telescope* (*INT*) at El Roque de los Muchachos observatory in visitor mode in 2019 July. We used the Intermediate Dispersion Spectrograph (IDS) and the R632V grating together with a 1 arcsec slit width. The spectra covered the ≃3500–6000 Å wavelength range at a resolving power of 2500 and were reduced/calibrated using the PAMELA/MOLLY softwares.

3.2.3 Telescopio Nazionale Galileo

Service mode observations were carried out at the Telescopio Nazionale Galileo at El Roque de los Muchachos observatory to acquire 106 MS high-resolution spectra. We used the High Accuracy Radial velocity Planet Searcher – North (HARPS-N; Cosentino et al.

[2]The MOLLY package is developed by Tom Marsh and is available at http://deneb.astro.warwick.ac.uk/phsaap/software.

2012) spectrograph together with the 1 arcsec fibre, resulting in the wavelength coverage of ≃3800–6900 Å. The resolving power of HARPS-N is 115 000. In order to wavelength calibrate the data, we used arc-lamp spectra taken with a second fibre. The data were reduced and calibrated using the automated HARPS-N pipeline.

3.2.4 Mercator telescope

We obtained 377 high-resolution MS spectra with the 1.2 m *Mercator* telescope located at the El Roque de los Muchachos observatory. We used the HERMES spectrograph (Raskin et al. 2011), which provided spectra covering the 3770–9000 Å range in a single exposure at a resolving power of 85 000. The observations were performed under the high-resolution mode and the data were reduced using the dedicated automated data reduction pipeline and radial velocity toolkit (HermesDRS).[3]

3.2.5 Xinglong 2.16m Telescope

Observations at the 2.16 metre telescope located at the Xinglong National Station (China) were performed in visitor mode during 2018 and 2019 to acquire 51 high-resolution MS spectra. We used the High Resolution fiber-fed Spectrograph (HRS; Fan et al. 2016), which provided echelle spectra covering the ≃3650–10 000 Å wavelength range at a resolving power of 49 800. Thorium-argon arc spectra were taken at the beginning and the end of each night. The data were reduced and calibrated using the IRAF package (Tody 1986).

4 METHODOLOGY AND RESULTS

In this section, we provide details on how we derive the WD ages and MS star metallicities, i.e. [Fe/H] abundances. The results are presented in Table 2 for the SDSS WD–MS binary sample and in Table 3 for the *Gaia* WD–MS CPMPs.

4.1 M dwarf metallicities of the SDSS WD–MS binary sample

We obtained the M dwarf [Fe/H] abundances from their *K*-band, near-infrared X-Shooter, and EMIR spectra following the procedure described in Newton et al. (2014). Note that at these wavelengths, the WD contributions are negligible (see Fig. 2). This method uses a semi-empirical multivariate linear regression based on the equivalent width of the 2205/2209 nm Na I absorption doublet to yield [Fe/H] values with an accuracy of 0.12 dex. To derive the equivalent width values, we corrected the systemic (radial) velocities and we normalized the fluxes in the 2194–2220 nm wavelength range fitting a third-order spline function. In this process, we excluded the Na I doublet absorption feature. We then used the trapezoidal rule to integrate the flux within the 2204–2210 nm region of the absorption doublet.

4.2 WD ages of the SDSS WD–MS binary sample

We first run a decomposition/fitting routine to the optical X-Shooter and OSIRIS spectra of the binaries to determine the spectral type of the M dwarfs and subtract their flux contribution (left-hand panels of Fig. 2, for details see Rebassa-Mansergas et al. 2007). The normalized Balmer lines of the residual WD spectra were then fitted with a grid of hydrogen-rich WD model atmosphere spectra (Koester 2010, and unpublished improvements) in order to measure $T_{\rm eff}$ and $\log g$ (see the right-hand panels of Fig. 2). When appropriate, we accounted for the 3D corrections provided by Tremblay et al. (2013) and, thus, we linearly interpolated these values in the cooling sequences developed by the La Plata Group for three different metallicities ($Z = 0.001$, Althaus et al. 2015; $Z = 0.01$, Renedo et al. 2010; and $Z = 0.02$, Camisassa et al. 2016) to obtain the WD masses and total ages, i.e. WD cooling plus MS progenitor lifetime.[4] The WD evolutionary sequences for $Z = 0.001$ and $Z = 0.02$ were derived from the full evolutionary history of their progenitor stars, from the Zero-Age-MS all the way to the WD phase. These WD models take into account all the relevant energy sources that govern the WD evolution, including the energy released by the crystallization process, as latent heat and as gravitational energy by the phase separation process. The progenitor lifetimes adopted in these sequences were interpolated from table 2 of Miller Bertolami (2016) and they adopted the initial-to-final mass relation of the same work, which is similar to the semi-empirical relations found in Catalán et al. (2008) and Cummings et al. (2018). The sequences of Renedo et al. (2010) for $Z = 0.01$ take into account all the relevant processes involved in the WD evolution, however they do not provide the progenitor lifetimes. We obtained those interpolating from table 2 of Miller Bertolami (2016).

Given that we know the [Fe/H] abundances (Section 4.1), and hence the Z values,[5] of the MS companions (assumed to be the same for the WD progenitors), we interpolated the measured Z between the three Z/total-age pairs obtained for each system from the evolutionary WD sequences to derive the corresponding total ages. In the cases where the metallicities were larger than 0.02 (the highest value provided by the models), we linearly extrapolated the ages from the cooling sequences of Camisassa et al. (2016). Taking into account the errors in effective temperature and surface gravity, we calculated the total age errors following the same approach.

It has to be emphasized that in this work we used a more updated set of cooling sequences as well as a different initial-to-final mass relation than in Rebassa-Mansergas et al. (2016b). Therefore, we have recalculated the total ages of the binaries studied in that work and included them in Table 2. Moreover, as indicated in Section 3.1.2, two SDSS WD–MS binaries were only observed by the GTC using the EMIR spectrograph. In these two cases, in order to obtain the total ages, we used the WD effective temperatures and surface gravities reported by Rebassa-Mansergas et al. (2016a), which were derived by fitting the optical SDSS publicly available spectra of these two binaries.

Of the 52 SDSS WD–MS binaries analysed here (23 from Rebassa-Mansergas et al. 2016b), 6 have masses $\lesssim 0.50\,{\rm M}_{\odot}$. Such low-mass WDs can not be formed via single stellar evolution because their progenitors have MS lifetimes longer than the Hubble time. Therefore, a binary origin involving mass transfer interactions is generally required to explain these objects (e.g. Rebassa-Mansergas et al. 2011). Because of this reason, we can not derive the ages of these six systems. A possibility is that these unresolved SDSS WD–MS binaries are in fact close binaries that evolved through a common envelope phase but have low inclinations, thus implying no radial

[3]Publicly available at http://www.mercator.iac.es/instruments/hermes/drs/

[4]The WD masses and cooling ages are practically identical in the three cases, however the MS progenitor lifetimes significantly vary as function of metallicity. Note also that for ultra-massive WDs, we used the sequence of Camisassa et al. (2019) for the three metallicities.

[5]We fitted a fifth order polynomial between [Fe/H] and Z conversions, calculated assuming Asplund, Grevesse & Sauval (2005) solar abundances, resulting in $Z = 0.01230 + 0.02560 \times [{\rm Fe/H}] + 0.03291 \times [{\rm Fe/H}]^2 + 0.02833 \times [{\rm Fe/H}]^3 + 0.01284 \times [{\rm Fe/H}]^4 + 0.00223 \times [{\rm Fe/H}]^5$.

Table 2. List of objects, RA and Dec. of the 52 SDSS WD–MS binaries containing hydrogen-rich WDs studied in this work. For 46 of them, we can derive the WD total ages. We also indicate the WD effective temperatures, surface gravities, and masses as well as the M dwarf spectral types (Sp) that have been obtained from our spectral fitting routine. The instruments used in the observations are indicated too. WD total ages and MS star [Fe/H] abundances are given in columns 8 and 9, respectively. The WD parameters of SDSSJ 0648+3810 and SDSSJ 2228+3912 are derived fitting the available SDSS spectra. The age and WD parameters age of SDSSJ 0138–0016 are obtained from Parsons et al. (2012).

Object	RA (deg)	Dec. (deg)	$T_{\rm eff}$ (WD) (K)	log g (WD) (dex)	Mass (WD) ($M_\odot$)	Sp (MS)	Age (Gyr)	[Fe/H] (dex)	Instr.
SDSSJ 0021–1103	5.491 25	− 11.058 78	10 718 ± 9	8.59 ± 0.03	$0.96^{+0.02}_{-0.01}$	M4	$1.35^{+0.09}_{-0.08}$	0.26 ± 0.12	X-Shooter
SDSSJ 0054+0057	13.577 25	0.962 81	19 729 ± 42	7.83 ± 0.01	$0.543^{+0.004}_{-0.004}$	M4	$4.731^{+0.010}_{-0.003}$	0.22 ± 0.12	X-Shooter
SDSSJ 0328+0017	52.178 83	0.297 14	12 885 ± 532	7.86 ± 0.13	$0.54^{+0.06}_{-0.05}$	M2	$8.51^{+3.48}_{-2.61}$	0.56 ± 0.12	X-Shooter
SDSSJ 0335+0038	53.952 42	0.642 28	17 993 ± 19	7.92 ± 0.01	$0.581^{+0.004}_{-0.004}$	M4	$3.62^{+0.39}_{-0.39}$	0.05 ± 0.12	X-Shooter
SDSSJ 1005+2112	151.264 21	21.201 11	20 658 ± 26	7.91 ± 0.01	$0.572^{+0.005}_{-0.005}$	M2	$4.14^{+0.1}_{-0.25}$	0.25 ± 0.12	X-Shooter
SDSSJ 1114+0838	168.580 33	8.641 40	11 752 ± 59	8.16 ± 0.03	$0.70^{+0.02}_{-0.02}$	M5	$0.98^{+0.04}_{-0.04}$	− 0.38 ± 0.12	X-Shooter
SDSSJ 1117+0129	169.396 33	1.494 39	9018 ± 10	8.25 ± 0.03	$0.74^{+0.02}_{-0.02}$	M6	$1.60^{+0.04}_{-0.02}$	0.15 ± 0.12	X-Shooter
SDSSJ 1120+1901	170.052 96	19.024 12	13 035 ± 1263	7.86 ± 0.24	$0.53^{+0.13}_{-0.10}$	M3	$8.00^{+4.00}_{-5.60}$	0.17 ± 0.12	X-Shooter
SDSSJ 1417+1301	214.417 58	13.030 14	34 682 ± 20	7.39 ± 0.01	$0.44^{+0.01}_{-0.01}$	M4	–	0.17 ± 0.12	X-Shooter
SDSSJ 1453+0010	223.274 05	0.180 08	12 025 ± 83	8.32 ± 0.03	$0.80^{+0.02}_{-0.02}$	M4	$0.86^{+0.06}_{-0.04}$	0.16 ± 0.12	X-Shooter
SDSSJ 1557+1442	239.336 22	14.704 91	12 165 ± 12	7.87 ± 0.03	$0.54^{+0.01}_{-0.01}$	M5	$8.67^{+2.14}_{-1.19}$	− 0.17 ± 0.12	X-Shooter
SDSSJ 1601+0505	240.402 92	5.091 08	44 479 ± 343	7.87 ± 0.03	$0.61^{+0.01}_{-0.01}$	M1	$1.82^{+0.38}_{-0.39}$	0.22 ± 0.12	X-Shooter
SDSSJ 1731+0703	262.768 86	7.062 51	11 888 ± 27	8.60 ± 0.03	$0.97^{+0.02}_{-0.02}$	M4	$1.04^{+0.06}_{-0.04}$	− 0.61 ± 0.12	X-Shooter
SDSSJ 2044–0614	311.131 00	− 6.244 50	16 792 ± 162	7.76 ± 0.03	$0.51^{+0.01}_{-0.01}$	M1	–	− 0.36 ± 0.12	X-Shooter
SDSSJ 2312+0053	348.128 29	0.889 33	29 181 ± 39	8.12 ± 0.02	$0.70^{+0.01}_{-0.01}$	M2	$0.43^{+0.03}_{-0.03}$	− 0.06 ± 0.12	X-Shooter
SDSSJ 2342+1559	355.60696	15.991 75	12 885 ± 45	8.06 ± 0.03	$0.64^{+0.02}_{-0.02}$	M5	$0.99^{+0.05}_{-0.05}$	− 0.61 ± 0.12	X-Shooter
SDSSJ 2350+0043	357.614 96	0.732 97	12 885 ± 2013	7.89 ± 0.35	$0.55^{+0.20}_{-0.15}$	M2	$6.61^{+5.39}_{-0.83}$	− 0.40 ± 0.12	X-Shooter
SDSSJ 0648+3810	102.053 19	38.168 31	20 098 ± 1341	7.97 ± 0.24	$0.61^{+0.13}_{-0.10}$	M1	$1.30^{+0.90}_{-1.29}$	− 0.55 ± 0.12	SDSS/EMIR
SDSSJ 1241+6007	190.419 85	60.119 85	23 076 ± 426	7.75 ± 0.07	$0.52^{+0.02}_{-0.02}$	M3	–	− 0.39 ± 0.12	Osiris/EMIR
SDSSJ 1510+4048	227.690 42	40.807 50	9573 ± 40	8.45 ± 0.07	$0.87^{+0.04}_{-0.05}$	M2	$1.50^{+0.16}_{-0.10}$	− 0.50 ± 0.12	Osiris/EMIR
SDSSJ 1521+2450	230.316 96	24.837 87	36 154 ± 149	7.91 ± 0.04	$0.61^{+0.02}_{-0.02}$	M2	$1.71^{+0.55}_{-1.22}$	0.19 ± 0.12	Osiris/EMIR
SDSSJ 1525+3629	231.324 54	36.495 89	9681 ± 35	7.61 ± 0.07	$0.42^{+0.03}_{-0.02}$	M4	–	− 0.3 ± 0.12	Osiris/EMIR
SDSSJ 1600+3626	240.249 29	36.436 08	23 076 ± 172	7.85 ± 0.03	$0.56^{+0.01}_{-0.01}$	M5	$5.05^{+1.66}_{-2.03}$	− 0.12 ± 0.12	Osiris/EMIR
SDSSJ 1605+4610	241.417 37	46.179 39	33 740 ± 280	7.97 ± 0.05	$0.64^{+0.03}_{-0.02}$	M0	$0.63^{+0.10}_{-0.12}$	− 0.78 ± 0.12	Osiris/EMIR
SDSSJ 1624+3217	246.204 17	32.283 89	89 774 ± 688	8.15 ± 0.07	$0.76^{+0.04}_{-0.04}$	M1	$0.06^{+0.06}_{-0.05}$	− 0.30 ± 0.12	Osiris/EMIR
SDSSJ 1624+3648	246.033 58	36.816 25	25 012 ± 205	7.99 ± 0.03	$0.63^{+0.01}_{-0.01}$	M3	$0.73^{+0.10}_{-0.25}$	− 0.36 ± 0.12	Osiris/EMIR
SDSSJ 1833+6431	278.371 62	64.531 04	54 094 ± 867	7.90 ± 0.05	$0.65^{+0.02}_{-0.02}$	M2	$0.59^{+0.08}_{-0.09}$	− 0.51 ± 0.12	Osiris/EMIR
SDSSJ 1834+4137	278.721 16	41.632 69	9456 ± 24	8.12 ± 0.05	$0.67^{+0.03}_{-0.03}$	M4	$1.42^{+0.03}_{-0.09}$	− 0.85 ± 0.12	Osiris/EMIR
SDSSJ 2228+3912	337.094 74	39.211 06	25 794 ± 1745	7.81 ± 0.24	$0.55^{+0.12}_{-0.08}$	M3	$7.23^{+4.71}_{-1.46}$	0.06 ± 0.12	SDSS/EMIR
SDSSJ 0003–0503*	0.987 23	− 5.059 09	19 967 ± 131	8.07 ± 0.02	$0.66^{+0.01}_{-0.01}$	M4	$0.72^{+0.11}_{-0.11}$	0.05 ± 0.12	X-Shooter
SDSSJ 0005–0544*	1.499 48	− 5.737 80	32 748 ± 224	7.73 ± 0.03	$0.53^{+0.01}_{-0.01}$	M2	$8.27^{+1.07}_{-0.28}$	0.06 ± 0.12	X-Shooter
SDSSJ 0036+0700*	9.010 79	7.013 11	36 105 ± 49	7.87 ± 0.02	$0.589^{+0.009}_{-0.009}$	M4	$3.89^{+0.94}_{-0.95}$	0.30 ± 0.12	X-Shooter
SDSSJ 0052–0051*	13.035 08	− 0.859 61	11 933 ± 94	8.02 ± 0.03	$0.61^{+0.02}_{-0.02}$	M4	$1.53^{+0.23}_{-0.52}$	0.06 ± 0.12	X-Shooter
SDSSJ 0111+0009*	17.849 54	0.159 81	12 326 ± 47	7.76 ± 0.03	$0.50^{+0.01}_{-0.01}$	M2	–	− 0.46 ± 0.12	X-Shooter
SDSSJ 0138–0016*	24.714 75	− 0.272 67	3570 ± 110	7.92 ± 0.02	$0.54^{+0.01}_{-0.01}$	M5	$9.50^{+0.30}_{-0.20}$	− 0.56 ± 0.12	X-Shooter
SDSSJ 0256–0730*	44.044 21	− 7.506 83	10 194 ± 68	8.84 ± 0.04	$1.09^{+0.02}_{-0.02}$	M5	$1.99^{+0.02}_{-0.02}$	− 0.27 ± 0.12	X-Shooter
SDSSJ 0258+0109*	44.57446	1.162 78	36 873 ± 123	7.75 ± 0.02	$0.540^{+0.007}_{-0.007}$	M3	$5.87^{+0.05}_{-0.39}$	0.23 ± 0.12	X-Shooter
SDSSJ 0321–0016*	50.402 25	− 0.275 11	31 096 ± 32	7.88 ± 0.02	$0.584^{+0.009}_{-0.008}$	M5	$2.95^{+0.88}_{-1.13}$	0.17 ± 0.12	X-Shooter
SDSSJ 0325–0111*	51.295 17	− 1.187 25	10 499 ± 14	8.13 ± 0.04	$0.68^{+0.02}_{-0.02}$	M2	$1.19^{+0.03}_{-0.04}$	− 0.36 ± 0.12	X-Shooter
SDSSJ 0331–0054*	52.883 83	− 0.914 83	30 742 ± 30	7.96 ± 0.01	$0.622^{+0.005}_{-0.005}$	M3	$1.07^{+0.08}_{-0.08}$	0.09 ± 0.12	X-Shooter
SDSSJ 0824+1723*	126.120 92	17.395 94	12 476 ± 52	7.86 ± 0.03	$0.54^{+0.01}_{-0.01}$	M3	$9.40^{+2.33}_{-0.47}$	− 0.10 ± 0.12	X-Shooter
SDSSJ 0832–0430*	128.230 02	− 4.512 85	16 064 ± 85	8.01 ± 0.01	$0.623^{+0.006}_{-0.005}$	M1	$0.85^{+0.02}_{-0.03}$	− 0.76 ± 0.12	X-Shooter
SDSSJ 0916–0031*	139.006 17	− 0.524 94	19 130 ± 63	8.30 ± 0.02	$0.79^{+0.01}_{-0.01}$	M4	$0.46^{+0.05}_{-0.01}$	0.30 ± 0.12	X-Shooter
SDSSJ 0933+0926*	143.299 62	9.445 08	30 401 ± 18	7.63 ± 0.01	$0.50^{+0.002}_{-0.002}$	M5	–	− 0.07 ± 0.12	X-Shooter
SDSSJ 1023+0427*	155.892 71	4.456 17	20 498 ± 68	7.89 ± 0.02	$0.56^{+0.01}_{-0.01}$	M4	$4.21^{+0.42}_{-0.21}$	0.18 ± 0.12	X-Shooter
SDSSJ 1040+0834*	160.239 50	8.572 67	10 254 ± 8	8.00 ± 0.03	$0.60^{+0.02}_{-0.02}$	M5	$1.55^{+0.23}_{-0.31}$	− 0.09 ± 0.12	X-Shooter
SDSSJ 1405+0409*	211.395 54	4.151 83	20 716 ± 88	8.15 ± 0.02	$0.71^{+0.02}_{-0.01}$	M4	$0.51^{+0.03}_{-0.03}$	− 0.30 ± 0.12	X-Shooter
SDSSJ 1527+1007*	231.933 79	10.122 89	34 079 ± 52	7.86 ± 0.02	$0.588^{+0.009}_{-0.009}$	M3	$1.31^{+0.24}_{-1.30}$	− 0.17 ± 0.12	X-Shooter

Table 2 – *continued*

Object	RA (deg)	Dec. (deg)	$T_{\rm eff}$ (WD) (K)	log g (WD) (dex)	Mass (WD) ($M_\odot$)	Sp (MS)	Age (Gyr)	[Fe/H] (dex)	Instr.
SDSSJ 1539+0922*	234.894 31	9.372 65	11 183 ± 143	8.72 ± 0.03	$1.04^{+0.02}_{-0.02}$	M5	$1.53^{+0.02}_{-0.01}$	0.29 ± 0.12	X-Shooter
SDSSJ 1558+0231*	239.721 71	2.527 31	30 062 ± 9	7.79 ± 0.01	$0.548^{+0.004}_{-0.003}$	M4	$7.24^{+0.38}_{-0.29}$	0.07 ± 0.12	X-Shooter
SDSSJ 1624–0022*	246.131 92	−0.380 06	26 291 ± 203	7.92 ± 0.03	$0.60^{+0.01}_{-0.01}$	M3	$1.40^{+0.30}_{-0.45}$	0.02 ± 0.12	X-Shooter
SDSSJ 2341–0947*	355.492 62	−9.787 94	9433 ± 26	8.27 ± 0.04	$0.76^{+0.02}_{-0.02}$	M4	$1.41^{+0.02}_{-0.02}$	0.07 ± 0.12	X-Shooter

Those systems that are reanalysed from Rebassa-Mansergas et al. (2016b) are indicated by * after their names.

Table 3. Object names, WD and MS coordinates, WD effective temperatures, surface gravities and masses measured from *Gaia* photometry and spectroscopy (when available), the corresponding total ages and the MS star [Fe/H] abundances (assumed to be same as for the WD progenitors) of the 235 *Gaia* WD–MS binaries analysed in this work. For 46 WDs, the masses are too low to derive an age. The complete table can be found in the supplementary material, where the *Gaia* source IDs of each component are also provided.

Object	WD RA/Dec. (deg)	MS RA/Dec (deg)	$T_{\rm eff\text{-}phot}$ (K)	log $g_{\rm phot}$ (dex)	$\rm Mass_{phot}$ ($M_\odot$)	$\rm Age_{phot}$ (Gyr)	$T_{\rm eff\text{-}spec}$ (K)	log $g_{\rm spec}$ (dex)	$\rm Mass_{spec}$ ($M_\odot$)	$\rm Age_{spec}$ (Gyr)	[Fe/H] (dex)
J0012+2328	2.961 63/23.486 78	3.006 12/23.471 78	8109 ± 210	8.17 ± 0.06	$0.70^{+0.04}_{-0.04}$	$1.77^{+0.10}_{-0.08}$	–	–	–	–	−0.18 ± 0.03
J0021+2531	5.317 79/25.526 27	5.316 96/25.524 31	9332 ± 126	8.49 ± 0.03	$0.90^{+0.02}_{-0.02}$	$1.57^{+0.02}_{-0.01}$	–	–	–	–	0.16 ± 0.05
J0033+4443	8.263 20/44.736 79	8.257 21/44.729 89	10 198 ± 164	7.98 ± 0.03	$0.59^{+0.02}_{-0.02}$	$1.99^{+0.48}_{-1.83}$	10141 ± 63	8.07 ± 0.06	$0.64^{+0.03}_{-0.04}$	$1.35^{+0.12}_{-0.29}$	-0.03 ± 0.02
J0045+1421	11.342 35/14.345 70	11.338 58/14.362 69	4886 ± 34	7.81 ± 0.02	$0.49^{+0.01}_{-0.01}$	–	–	–	–	–	−0.26 ± 0.03
J0048+1333	12.182 30/13.557 94	12.180 96/13.555 89	12 588 ± 1543	8.45 ± 0.14	$0.88^{+0.09}_{-0.09}$	$0.65^{+0.06}_{-0.38}$	–	–	–	–	0.27 ± 0.5
J0055+3321	13.813 36/33.351 59	13.816 54/33.352 14	18 190 ± 1274	7.90 ± 0.08	$0.55^{+0.04}_{-0.04}$	$6.50^{+2.60}_{-5.80}$	–	–	–	–	0.42 ± 0.04
J0103+6108	15.794 64/61.128 71	15.792 92/61.135 67	9317 ± 270	8.02 ± 0.06	$0.61^{+0.03}_{-0.03}$	$1.48^{+0.14}_{-1.36}$	–	–	–	–	−0.10 ± 0.03
J0108+7018	17.121 71/70.300 84	17.137 25/70.300 42	5351 ± 154	7.93 ± 0.09	$0.55^{+0.05}_{-0.04}$	$10.21^{+1.79}_{-2.83}$	–	–	–	–	−0.11 ± 0.04
J0112+0454	18.035 88/ 4.919 14	18.033 63/ 4.916 25	19 160 ± 744	8.07 ± 0.04	$0.66^{+0.02}_{-0.02}$	$0.68^{+0.13}_{-0.15}$	20098 ± 211	8.06 ± 0.04	$0.65^{+0.02}_{-0.02}$	$0.69^{+0.13}_{-0.13}$	−0.03 ± 0.04
J0115+1534	18.983 83/15.580 56	18.982 04/15.580 08	24 039 ± 577	7.95 ± 0.02	$0.59^{+0.01}_{-0.01}$	$5.65^{+1.20}_{-1.03}$	–	–	–	–	0.63 ± 0.13
J0119+6218	19.835 86/62.301 48	19.834 71/62.305 39	16 166 ± 336	7.94 ± 0.03	$0.57^{+0.02}_{-0.01}$	$7.55^{+2.21}_{-0.14}$	–	–	–	–	0.41 ± 0.03

velocity variation detection. This issue will be further discussed in Section 5.

4.3 MS metallicities of the *Gaia* WD–MS CPMP sample

We obtained 534 high-resolution spectra (Table 1) of 349 unique companion stars in our sample,[6] 26 of which have spectral types earlier than ≃F0, 260 are F-, G-, or K-type stars, 6 are giants of luminosity class between III and IV, and 55 are M dwarfs (45 of spectral type M3 or earlier and 10 of spectral types M4-M5). The lack of near-infrared spectroscopy does not allow measuring the [Fe/H] abundances of the M dwarfs in the same way as we have performed for the SDSS sample. Hence, we attempted to measure the abundances of the 311 F, G, K, and early M (M3 or earlier) as well as giant companions via detailed spectroscopic fits.

We determined the effective temperatures, surface gravities, microturbulent velocities, and [Fe/H] abundances using the TGVIT code (Takeda et al. 2005). This routine implements the iron ionization plus the iron equilibrium conditions as well as match of the curve of growth. Such a methodology is widely applied to solar-type stars of spectral types between F5 and K2/K3. We used a set of well-defined 302 Fe I and 28 Fe II lines in the analysis. The code makes use of ATLAS9, plane-parallel, local thermodynamic equilibrium atmosphere models (Kurucz 1993). Uncertainties in the stellar parameters are statistical, that is, each stellar parameter is progressively changed from the converged solution until a value in which any of the aforementioned conditions is no longer fulfilled.

For low-mass stars, M dwarfs, we determined the stellar parameters using the procedures developed by Maldonado et al. (2015).[7] In brief, this routine uses as a temperature diagnostic the ratios of pseudo-equivalent widths of spectral features, while calibrations for the stellar metallicity are derived from combinations and ratios of features. The temperatures and metallicities thus derived are used together with photometric estimates of surface gravity, mass, and radius to calibrate empirical relations for these parameters.

The procedures described above converged to reliable fits in 235 of the cases. These companions stars are illustrated as black solid dots, as well as their WD primaries, in Fig. 1. For the remaining 76 objects, the available spectra were of too low signal-to-noise ratio ($\lesssim$30), the number of measured Fe lines were too low, or there were problems in measuring and correcting the radial velocity for a proper determination of the [Fe/H] abundances. For those objects with more than one [Fe/H] determination from available multiple spectra, we used the average values. In the few cases, where the individual [Fe/H] values considerably disagreed, we adopted the value corresponding to the spectrum with higher signal-to-noise ratio.

4.4 WD ages of the *Gaia* WD–MS CPMP sample

Low-resolution optical spectra were obtained for 214 WDs at the *WHT* and *INT* telescopes (Table 1), however only 67 of their companions have available high-resolution MS spectra (Section 4.3). Of these 67 WDs, 15 are hydrogen-rich (DA) WDs that unfortunately have too noisy spectra for measurement of reliable stellar parameters, 14 are featureless (DC) WDs, 3 are helium-rich (DB) WDs, 1 is a metal-rich (DZ) WD, and only 34 are hydrogen-rich (DA) WDs with good fits to their spectra. This implies we can only attempt to determine ages for 34 of the 235 binaries for which we have obtained a metallicity value (Section 4.3). As a consequence, rather than measuring the WD stellar parameters (hence ages) from their available good-quality spectra, we decided to derive them using the

[6]Several targets were observed more than once at the same and/or different telescopes.
[7]https://github.com/jesusmaldonadoprado/mdslines

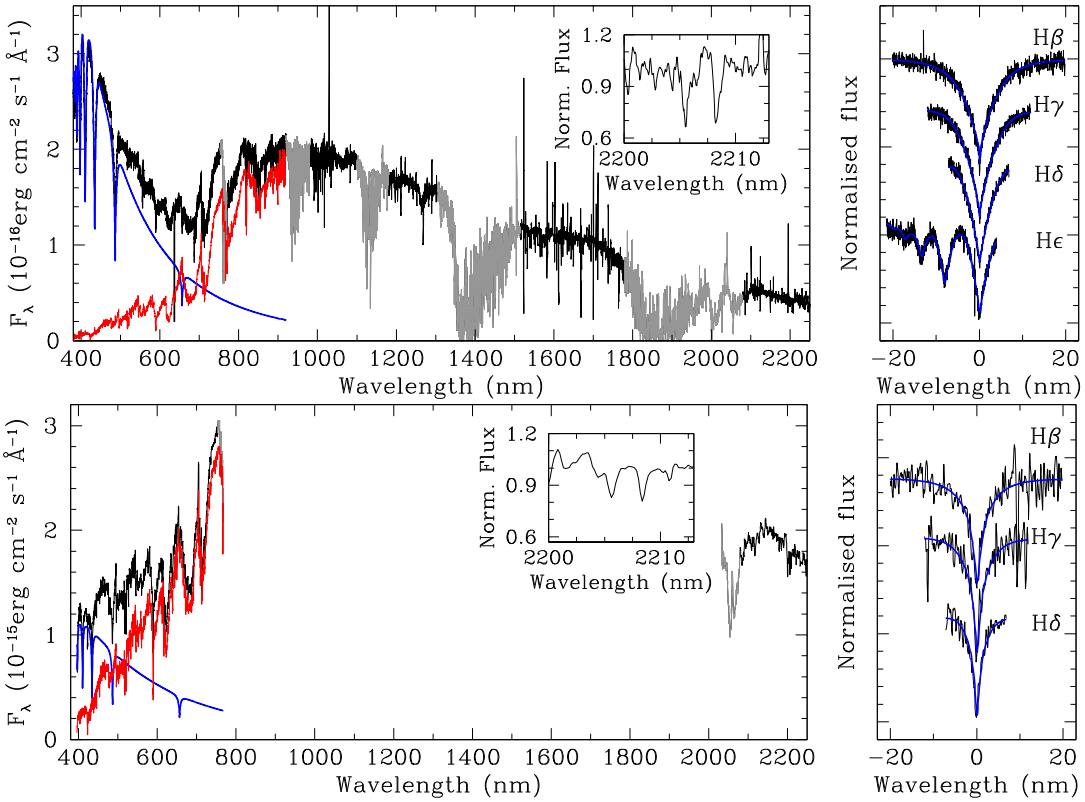

Figure 2. Top-left panel: spectrum of SDSSJ 0335+0038 (black) taken with X-Shooter. The telluric absorption regions are shown in grey. At blue wavelengths (λ <600 nm) the flux contribution is dominated by the WD. Conversely, the red and near-infrared regions are dominated by the flux of the MS companion. In blue and red solid lines, we show the best-fitting WD model and MS star template, respectively. The top right corner shows the 2205/2209 nm Na I absorption doublet (free of telluric absorption) used to estimate the [Fe/H] abundance of the MS star. Top-right panel: the normalized residual and normalized WD Balmer lines (black) resulting from subtracting the MS star together with the WD model (blue) that best fits the spectrum. Bottom panels: the same but for SDSSJ 1510+4048, which was observed with OSIRIS and EMIR mounted at the GTC. Note that the EMIR spectrum in the near-infrared is not flux calibrated and has been normalized to the average optical flux.

corresponding *Gaia* EDR3 (Gaia Collaboration 2021; Riello et al. 2020) photometry and parallaxes.[8] Compared to using spectroscopy alone, this holds the potential of providing a factor $\simeq$7 increase in the number of age–metallicity pairs.

All the WDs that are part of our *Gaia* WD–MS CPMPs are associated to measured parallaxes and G, $G_{\rm BP}$, and $G_{\rm RP}$ magnitudes from *Gaia* EDR3. This allowed for derivations of the corresponding effective temperatures and surface gravities, hence masses and ages, by interpolating the observed G absolute magnitudes and $G_{\rm BP}-G_{\rm RP}$ colours in the cooling sequences developed by the La Plata group for pure-hydrogen atmospheres (see Section 4.2). The synthetic G, $G_{\rm BP}$ and $G_{\rm RP}$ absolute magnitudes were incorporated by us to the WD cooling sequences integrating the flux of the associated model atmosphere spectra (Koester 2010) over the corresponding EDR3 pass-bands. It has to be emphasized that before performing the interpolation, the observed EDR3 magnitudes were corrected from extinction using the 3D maps of Lallement et al. (2014) and Capitanio et al. (2017). As expected from their close distance, the extinction correction was rather low in most cases with an average value of $A_{\rm g}$ = 0.04 mag and a maximum correction of $A_{\rm g}$ = 0.26 mag, where $A_{\rm g}$ was obtained from $A_{\rm V}$ using the law of Fitzpatrick et al. (2019) and assuming $R_{\rm V}$ = 3.1. The effective temperature and surface gravity errors were obtained by propagating the parallax and photometric errors.

It is important to note that we find a relatively large fraction ($\simeq$19 per cent) of low-mass ($\lesssim$0.5 $M_{\odot}$) WDs. This is intriguing since these are in resolved CPMP systems and their progenitors should have evolved like single stars, hence producing higher mass WDs. Half of the these presumably low-mass WDs have photometric effective temperatures under $\simeq$6000 K, hence they could be non-DA WDs for which the age we measure is uncertain. A systematic shift towards low masses below $\simeq$6000 K has also been reported by McCleery et al. (2020). For the hotter WDs, pure-helium DB models would yield even lower masses. Hence, a possible explanation is that the atmospheres of these WDs are not hydrogen nor helium dominated. Another possibility is that these objects are, or were, triple systems formed by an inner close binary (for example a double degenerate) and an outer MS companion. We will investigate these hypotheses in a separate publication.

An obvious question is whether the stellar parameters measured using both methods (spectroscopy and photometry) are consistent. To check this, we derived the effective temperatures and surface gravities of 107 hydrogen-rich DA WDs that we observed at the *WHT* and *INT* in the same way as described in Section 4.2 (without the need of subtracting the MS companion contribution, since these are resolved WDs in CPMPs). Hereafter, we consider $T_{\rm eff\text{-}spec}$ and $\log(g)_{\rm spec}$ as the measured values from spectroscopy. The photometric parameters, $T_{\rm eff\text{-}phot}$ and $\log g_{\rm phot}$, were derived as described in the

[8]Note that the *Gaia* WD–MS CPMPs were selected using DR2 data (Fig. 1). However, we used the newest EDR3 to measure the WD ages.

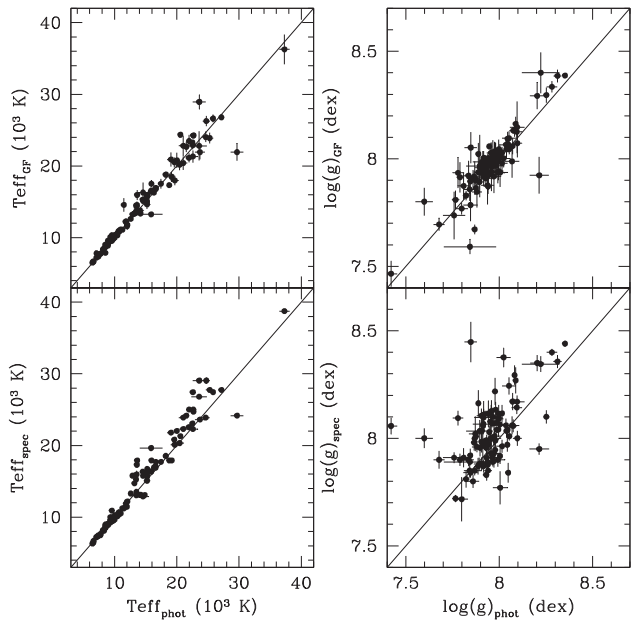

Figure 3. Top panels: a comparison between the WD effective temperatures (left) and surface gravities (right) measured in this work from *Gaia* EDR3 photometry and parallaxes as compared to those obtained by Gentile Fusillo et al. (2019) from *Gaia* DR2 data. Bottom panels: the same but comparing the photometric EDR3 values to those obtained from our follow-up spectroscopy.

previous paragraphs from the available *Gaia* EDR3 data. In the bottom panels of Fig. 3, we compare the stellar parameters thus obtained. If we define τ as

$$\tau = \frac{|\text{spec value} - \text{phot value}|}{\sqrt{\text{spec}\,\sigma^2 + \text{phot}\,\sigma^2}}, \quad (1)$$

where 'value' indicates either effective temperature of surface gravity and σ the corresponding errors, we find that the $T_{\rm eff}$ and $\log g$ measurements are consistent within 2τ for $\simeq$30 and $\simeq$50 per cent of the cases, respectively. Tremblay et al. (2020) argued that the photometric effective temperatures they measured for a sample of 89 *Gaia* DR2 hydrogen-rich WDs within 40 pc were 2.7 per cent underestimated as compared to their spectroscopic measurements. By considering this effect, the percentage of WDs with consistent spectroscopic and photometric effective temperatures in our sample increases from $\simeq$30 per cent to $\simeq$45 per cent. The percentages of agreement within 2τ further increase to $\simeq$70 per cent for both $T_{\rm eff}$ and $\log g$ if we systematically add a 0.015 dex uncertainty to the $\log g$ measurements and a 150 K uncertainty to the effective temperature values. This clearly reveals the effect the small errors in our measurements have in quantifying the degree of consistency between the two methods. We thus conclude that the spectroscopic and photometric measurements are broadly consistent. We will further discuss this issue in Section 5.

For completeness, we show in the top panels of Fig. 3 the comparison between our photometric values and those obtained from *Gaia* DR2 data by Gentile Fusillo et al. (2019). Visual inspection suggests the two sets of data are in good agreement. Indeed, in $\simeq$75/85 per cent of the cases the effective temperature/surface gravity measurements are consistent within 2τ.

5 DISCUSSION: THE AGE–METALLICITY RELATION

The AMR that results from the SDSS WD–MS binary sample is shown in the top left panel of Fig. 4, where a clear scatter of [Fe/H] abundances (>0.2 dex) is observed at most ages. This is corroborated in the bottom left panel of the same figure, where we show the average [Fe/H] per 1 Gyr bin. It is worth noting that in $\simeq$20 per cent of the cases the age measurements are subjected to substantial uncertainties (>30 per cent of relative error; grey points in Fig. 4). This is due to the relatively large uncertainties in the measured WD parameters that translate into larger age uncertainties and, mainly, due to the fact that the determined WD masses are low ($\lesssim$0.55 $M_\odot$). The lower the WD mass, the longer its progenitor spent on the MS. This MS lifetime is very sensitive to the mass of the WD progenitor star, thus even small errors in the derived WD masses translate into rather different ages spent on the MS and, as a consequence, into larger total age uncertainties. Given that low-mass WDs evolve from low-mass MS stars that require a longer time to leave the MS, the percentage of ages with larger uncertainties is higher for intermediate and old ages ($\gtrsim$5 Gyr).

It is also important to mention that these unresolved SDSS WD–MS binaries are expected to have evolved avoiding mass transfer episodes based on the lack of radial velocity variations. However, as discussed in Section 4.2, it is possible that a small number of the SDSS WD–MS systems are in fact post common envelope binaries with low orbital inclinations (preventing the detection of radial velocity variations). For those systems, the measured ages would not be accurate. The probability of non-detection of a close WD–MS binary due to a low-inclination is $\simeq$15 per cent (Nebot Gómez-Morán et al. 2011). This could explain why the three most metal-poor stars in the sample ([Fe/H]<−0.7 dex) appear to be younger than 2 Gyrs.

The *Gaia* WD–MS CPMP AMR is illustrated in the top right panel of Fig. 4 and the corresponding average [Fe/H] per 1 Gyr bin in the bottom right panel. In the same way as we have observed for the SDSS sample, the scatter of [Fe/H] abundances becomes apparent at all ages. It has to be noted that the WD ages for this sample were obtained from the available *Gaia* EDR3 photometry and that the WD stellar parameters obtained from these data are found to be broadly consistent with those obtained from the spectroscopic fits (Section 4.4). To investigate whether or not this issue affects the result obtained, we derived the (spectroscopic) WD ages of the 34 DA WDs for which the stellar parameters are also measured from spectroscopy (Section 4.4). These values are included in Table 3. We found the same scatter of [Fe/H] despite the fact that the individual ages vary, as expected, for some objects. Therefore, we can safely conclude that the scatter of metallicities in the *Gaia* WD–MS CPMP AMR is real.

It is also important to emphasize that the WD cooling sequences we have adopted to determine the stellar parameters are those developed for hydrogen-rich DA WDs. The lack of spectroscopy does not allow us to confirm this assumption for those WDs with only *Gaia* photometry available. Thus, we expect a fraction of non-DA WDs in our sample. From our spectroscopic sub-sample of 67 objects, we calculate fractions of $\simeq$73 per cent DAs, $\simeq$4 per cent DBs, $\simeq$1 per cent DZs, and $\simeq$20 per cent DCs, although the latter (visual) classification is likely biased because of signal-to-noise ratio issues of the spectra. Assuming these fractions are the same for the entire *Gaia* WD–MS CPMP sample, we reach the following conclusions: (i) $\simeq$4 per cent of our ages are underestimated because we are using pure-hydrogen sequences to derive the ages of DB WDs. This is because photometric masses obtained assuming pure-helium DB sequences

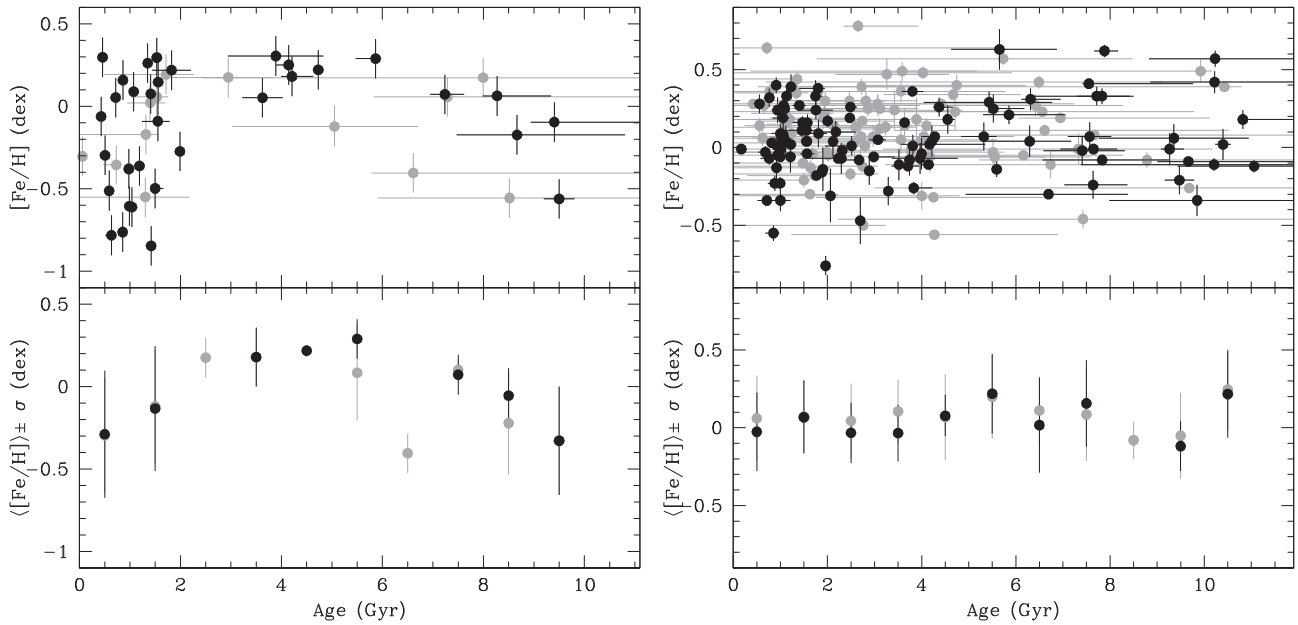

Figure 4. Top left panel: the AMR obtained from SDSS WD–MS binaries. Black dots represent ages with relative errors less than 30 per cent. Bottom left panel: average [Fe/H] values for 1 Gyr bins, together with their standard deviations for the entire sample (grey) and for the sample with age relative errors below 30 per cent (black). Right-hand panels: the same but for *Gaia* WD–MS CPMPs.

are generally lower than those obtained using pure-hydrogen models (Gentile Fusillo et al. 2019). This implies lower MS progenitor masses and larger progenitor lifetimes as compared to those obtained using pure-hydrogen models; (ii) given that ≃40 per cent of WDs have He-rich atmospheres at ≃5000–7000 K (McCleery et al. 2020), we expect approximately half of the spectroscopically (visually) classified objects as DC WDs to have He-dominated atmospheres. This implies an additional ≃10 per cent of underestimated ages in the total sample; (iii) ≃1 per cent of the WDs are expected to have other atmospheric composition apart from hydrogen and helium, such as DZ WDs. In these cases, the derived ages are uncertain. In summary, we expect ≃14 per cent of the *Gaia* WD–MS CPMP ages to be underestimated and ≃1 per cent to be uncertain.

In the top left panel of Fig. 5, we show the AMR that results from combining our SDSS and the full *Gaia* WD–MS binary samples, a total of 235 age-[Fe/H] pairs. The average [Fe/H] abundances per Gyr bin and the standard deviations are shown in the left bottom panel of the same figure and provided in Table 4. The sample is dominated by young objects ($\lesssim$5 Gyr; see bottom right panel of Fig. 5), but it also samples both intermediate and old ages. Unfortunately, very few objects in our total sample have ages larger than 10 Gyr, which does not allow us to study the properties of the AMR relation for very old ages in a robust way. The drop of systems with ages >10 Gyr can be understood as follows. In order to achieve an age longer than 10 Gyrs, a WD requires one of the following properties: (1) a very low mass ($\simeq$0.5 $M_\odot$) thus implying a very long MS progenitor lifetime and a short cooling age (hence a relatively hot tempreature; >10 000 K); (2) a very cool effective temperature (≤4000 K), thus implying a long cooling age and a short progenitor lifetime (hence a relatively more massive WD; $\gtrsim$0.6 $M_\odot$); (3) a low mass ($\simeq$0.55 $M_\odot$) and a low effective temperature (∼6000 K). As explained in Section 2, the SDSS WD–MS sample suffers from selection effects against cool WDs and therefore the probability for detecting very old age systems decreases. For the *Gaia* population, we are analysing objects with average distances of 150 pc (Section 2), which defines a sample close to be volume limited. In a volume-limited sample, not only hot WDs (>10 000 K) are intrinsically less numerous but also the completeness of cold (<5000 K) and less luminous WDs decreases to ≃60 per cent (Torres et al. 2021). These effects imply that, overall, it becomes intrinsically more difficult to find WDs with ages longer than 10 Gyrs.

Like Casagrande et al. (2011), we find no steep decline in metallicity for ages in the ≃9–10 Gyr range, a trend that was reported by Bergemann et al. (2014). The AMR we obtained fluctuates between approximately −0.5 and +0.5 dex with a peak centred at around [Fe/H]=0 (see the top right panel of Fig. 5) and, as expected from the previous discussion, it does not show any apparent correlation. This result is in agreement with several previous studies that analysed the AMR in which the ages were derived from Strömgren photometry (Feltzing, Holmberg & Hurley 2001; Nordström et al. 2004; Casagrande et al. 2011), spectroscopy and luminosities obtained via parallaxes (Buder et al. 2019; Delgado Mena et al. 2019; Nissen et al. 2020), isochrone matching (Hayden et al. 2020), open clusters (Carraro, Ng & Portinari 1998; Pancino et al. 2010), and asteroseismology (Silva Aguirre et al. 2018; Miglio et al. 2021). The analysis performed in this work using a different technique for measuring stellar ages reaches the same conclusion. Self-enrichment of gas in star-forming regions (Pilyugin & Edmunds 1996) or episodic gas in-fall on to the disc (Köppen & Hensler 2005) are proposed physical mechanisms to explain the lack of correlation between age and metallicity in the solar neighbourhood. However, the most accepted scenario invokes radial migration, a physical mechanism in which metal-rich stars that form in the inner disc migrate to the outer and metal-poorer disc (Sellwood & Binney 2002; Roškar et al. 2008; Minchev et al. 2011; Minchev, Chiappini & Martig 2013; Feuillet et al. 2019). The validity of this scenario is further supported by the fact that our AMR displays young (≃1 Gyr) but metal-rich ([Fe/H]>2 dex) objects (left-hand panel of Fig. 5). It is widely accepted that such stars cannot form in the solar neighbourhood and, as a consequece, must have migrated from a

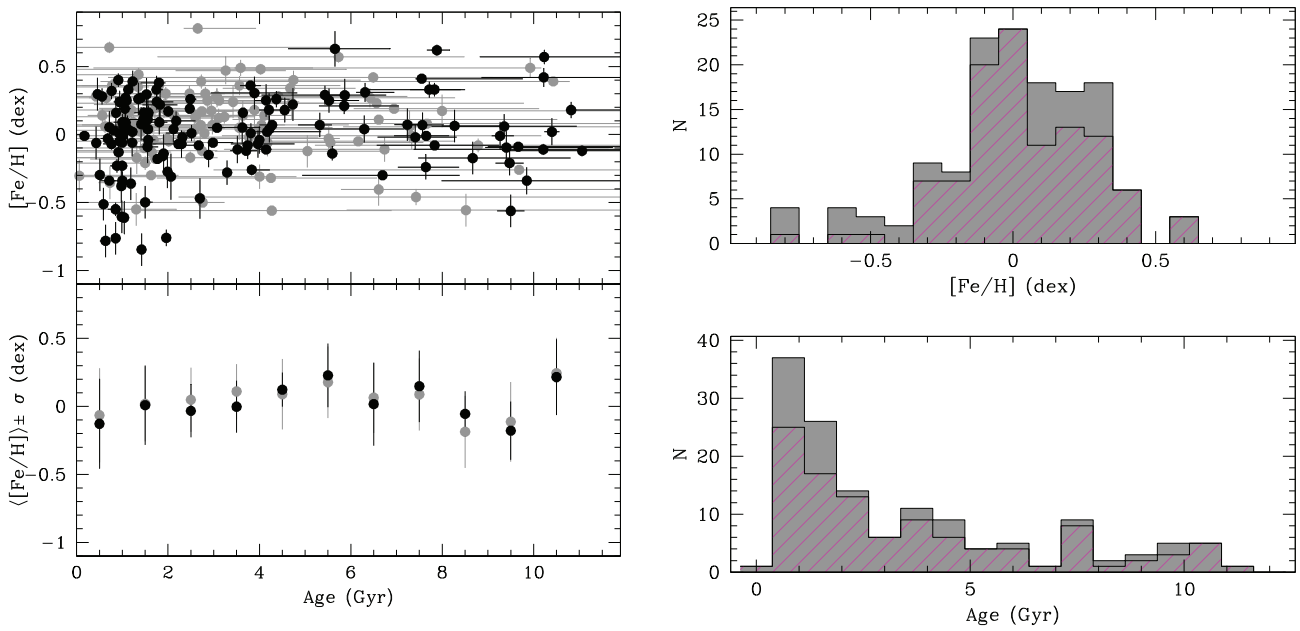

Figure 5. Left-hand panels: the same as Fig. 4 but for the entire sample studied in this work (46 SDSS WD–MS binaries plus 189 *Gaia* WD–MS CPMPs). There is no correlation between age and metallicity. Right-hand panels: the age (bottom; relative error less than 30 per cent) and [Fe/H] abundance (top) corresponding distributions. For comparative purposes, the age and [Fe/H] abundance distributions for the *Gaia* WD–MS binary sample are shown in magenta.

Table 4. $\langle$[Fe/H]$\rangle \pm \sigma$ for 1 Gyr bins obtained from the full WD–MS binary sample studied in this work. Only the age values with relative uncertainties under 30 per cent have been considered (black solid dots in the bottom panel of Fig. 5). For completeness, we also provide the values for the *Gaia* and SDSS samples.

Age (Gyr)	Full sample $\langle$[Fe/H]$\rangle \pm \sigma$ (dex)	*Gaia* sample $\langle$[Fe/H]$\rangle \pm \sigma$ (dex)	SDSS sample $\langle$[Fe/H]$\rangle \pm \sigma$ (dex)
0.5	−0.13 ± 0.33	−0.03 ± 0.25	−0.29 ± 0.39
1.5	0.01 ± 0.29	0.07 ± 0.23	−0.13 ± 0.38
2.5	−0.03 ± 0.19	−0.03 ± 0.19	–
3.5	0.00 ± 0.19	−0.03 ± 0.18	0.18 ± 0.18
4.5	0.12 ± 0.13	0.08 ± 0.13	0.22 ± 0.03
5.5	0.23 ± 0.23	0.22 ± 0.26	0.29 ± 0.12
6.5	0.02 ± 0.31	0.02 ± 0.31	–
7.5	0.15 ± 0.26	0.16 ± 0.28	0.07 ± 0.12
8.5	−0.06 ± 0.17	–	−0.06 ± 0.17
9.5	−0.18 ± 0.21	−0.12 ± 0.16	−0.33 ± 0.33
10.5	0.22 ± 0.28	0.22 ± 0.28	–

more metal-rich enviroment in the inner Galaxy (Haywood 2008; Brunetti, Chiappini & Pfenniger 2011).

6 CONCLUSIONS

Dating a star is a challenging task. For decades, this difficult endeavour has been pursued for single stars using different techniques, which has allowed analysing the observational properties of the AMR in the solar neighbourhood. These studies seem to converge to the same result, i.e. there is no correlation between age and metallicity as traced by the [Fe/H] abundances. In this work, we have used an alternative way for measuring stellar ages based on the analysis of WD–MS binaries from which we can obtain accurate WD ages and MS [Fe/H] abundances. The AMR that we have obtained displays a scatter of approximately ±0.5 dex at all ages. This is yet another robust confirmation of the lack of correlation between age and metallicity in the solar neighbourhood.

ACKNOWLEDGEMENTS

Project supported by a 2019 Leonardo Grant for Researchers and Cultural Creators, BBVA Foundation. The Foundation accepts no responsibility for the opinions, statements, and contents included in the project and/or the results thereof, which are entirely the responsibility of the authors.

ARM acknowledges additional support from the MINECO under the Ramón y Cajal program (RYC-2016-20254). JM acknowledges support from the Accordo Attuativo ASI-INAF n. 2018.22.HH.O, Partecipazione alla fase B1 della missione Ariel. RR has received funding from the postdoctoral fellowship programme Beatriu de Pinós, funded by the AGAUR (Secretary of Universities and Research, Government of Catalonia) and by the Horizon 2020 programme of research and innovation of the European Union under the MSCA (MarieC Skłodowska-Curie Actions) grant agreement no. 801370. ST acknowledges support from the MINECO under the AYA2017-86274-P grant, and the AGAUR grant SGR-661/2017. MJH was supported by the UK Science and Technology Facilities Council studentship ST/R505195/1. BTG was supported by a Leverhulme Research Fellowship and the UK STFC grant ST/T000406/1. PET, TC, and MH have received funding from the European Research Council under the European Union's Horizon 2020 research and innovation programme n. 677706 (WD3D).

Based on observations made with the Gran Telescopio Canarias (GTC; programmes GTC6-16B, GTC1-17A, GTC26-17B, and GTC6-18A), installed in the Spanish Observatorio del Roque de los Muchachos of the Instituto de Astrofísica de Canarias, in the island of La Palma. This work is based on observations made with ESO Telescopes at the La Silla Paranal Observatory under programme ID 0101.B-0130. Based on observations made with the Telescopio Nazionale Galileo and Mercator Telescope awarded to

the International Time Programme ITP18_8. Based on observations made with the William Herschel Telescope (programmes C12 and C26) and Isaac Newton Telescope (programme P4W) operated on the island of La Palma by the Isaac Newton Group of Telescopes in the Spanish Observatorio del Roque de los Muchachos of the Instituto de Astrofísica de Canarias. We acknowledge the support of the staff of the Xinglong 2.16 m telescope. This work was partially supported by the Open Project Program of the Key Laboratory of Optical Astronomy, National Astronomical Observatories, Chinese Academy of Sciences.

MJH acknowledges Saskia Prins, the support astronomer at Mercator for her invaluable help.

This work has made use of data from the European Space Agency (ESA) mission *Gaia* (https://www.cosmos.esa.int/gaia), processed by the *Gaia* Data Processing and Analysis Consortium (DPAC, https://www.cosmos.esa.int/web/gaia/dpac/consortium). Funding for the DPAC has been provided by national institutions, in particular the institutions participating in the *Gaia* Multilateral Agreement.

DATA AVAILABILITY

The data underlying this article are available in the manuscript. Supplementary material will be shared on reasonable request to the corresponding author.

REFERENCES

Althaus L. G., Camisassa M. E., Miller Bertolami M. M., Córsico A. H., García-Berro E., 2015, A&A, 576, A9
Althaus L. G., Córsico A. H., Isern J., García-Berro E., 2010, A&AR, 18, 471
Andrews J. J., Chanamé J., Agüeros M. A., 2017, MNRAS, 472, 675
Asplund M., Grevesse N., Sauval A. J., 2005, in Barnes T. G. III, Bash F. N., eds, ASP Conf. Ser. Vol. 336, Cosmic Abundances as Records of Stellar Evolution and Nucleosynthesis. Astron. Soc. Pac., San Franscisco, p. 25
Barrientos M., Chanamé J., 2021, preprint (arXiv:2102.07790)
Barry D. C., 1988, ApJ, 334, 436
Bensby T., Feltzing S., Oey M. S., 2014, A&A, 562, A71
Bergemann M. et al., 2014, A&A, 565, A89
Brunetti M., Chiappini C., Pfenniger D., 2011, A&A, 534, A75
Buder S. et al., 2019, A&A, 624, A19
Camisassa M. E., Althaus L. G., Córsico A. H., Vinyoles N., Serenelli A. M., Isern J., Miller Bertolami M. M., García-Berro E., 2016, ApJ, 823, 158
Camisassa M. E. et al., 2019, A&A, 625, A87
Capitanio L., Lallement R., Vergely J. L., Elyajouri M., Monreal-Ibero A., 2017, A&A, 606, A65
Carraro G., Ng Y. K., Portinari L., 1998, MNRAS, 296, 1045
Casagrande L., Schönrich R., Asplund M., Cassisi S., Ramírez I., Meléndez J., Bensby T., Feltzing S., 2011, A&A, 530, A138
Casagrande L. et al., 2016, MNRAS, 455, 987
Catalán S., Isern J., García-Berro E., Ribas I., 2008, MNRAS, 387, 1693
Cosentino R. et al., 2012, in McLean I. S., Ramsay S. K., Takami H., eds, SPIE Conf. Ser. Vol. 8446, Ground-based and Airborne Instrumentation for Astronomy IV. SPIE, Bellingham, p. 84461V
Cummings J. D., Kalirai J. S., Tremblay P. E., Ramirez-Ruiz E., Choi J., 2018, ApJ, 866, 21
Delgado Mena E. et al., 2019, A&A, 624, A78
Edvardsson B., Andersen J., Gustafsson B., Lambert D. L., Nissen P. E., Tomkin J., 1993, A&A, 275, 101
Eisenstein D. J. et al., 2011, AJ, 142, 72
El-Badry K., Rix H.-W., 2018, MNRAS, 480, 4884
El-Badry K., Rix H.-W., Heintz T. M., 2021, MNRAS, preprint (arXiv:2101.05282)
Fan Z. et al., 2016, PASP, 128, 115005
Feltzing S., Chiba M., 2013, New Astron. Rev., 57, 80
Feltzing S., Holmberg J., Hurley J. R., 2001, A&A, 377, 911
Feuillet D. K., Frankel N., Lind K., Frinchaboy P. M., García-Hernández D. A., Lane R. R., Nitschelm C., Roman-Lopes A., 2019, MNRAS, 489, 1742
Fitzpatrick E. L., Massa D., Gordon K. D., Bohlin R., Clayton G. C., 2019, ApJ, 886, 108
Fouesneau M., Rix H.-W., von Hippel T., Hogg D. W., Tian H., 2019, ApJ, 870, 9
Gaia Collaboration, 2016, A&A, 595, A1
Gaia Collaboration, 2018a, A&A, 616, A1
Gaia Collaboration, 2018b, A&A, 616, A10
Gaia Collaboration, 2021, A&A, 649A, 1G
Gentile Fusillo N. P. et al., 2019, MNRAS, 482, 4570
Hayden M. R. et al., 2020, preprint (arXiv:2011.13745)
Haywood M., 2008, MNRAS, 388, 1175
Haywood M., Di Matteo P., Lehnert M. D., Katz D., Gómez A., 2013, A&A, 560, A109
Holtzman J. A. et al., 2015, AJ, 150, 148
Howes L. M., Lindegren L., Feltzing S., Church R. P., Bensby T., 2019, A&A, 622, A27
Jiménez-Esteban F. M., Solano E., Rodrigo C., 2019, AJ, 157, 78
Jørgensen B. R., Lindegren L., 2005, A&A, 436, 127
Koester D., 2010, Mem. Soc. Astron. Ital., 81, 921
Köppen J., Hensler G., 2005, A&A, 434, 531
Kurucz R., 1993, ATLAS9 Stellar Atmosphere Programs and 2 km/s grid. ATLAS9 Stellar Atmosphere Programs and 2 km/s grid. Kurucz CD-ROM No. 13. Cambridge, Mass.: Smithsonian Astrophysical Observatory,
Kurucz R., 1993, ATLAS9 Stellar Atmosphere Programs and 2 km/s grid. Kurucz CD-ROM No. 13. Cambridge, p. 13
Lallement R., Vergely J. L., Valette B., Puspitarini L., Eyer L., Casagrande L., 2014, A&A, 561, A91
Lam M. C., Hambly N. C., Lodieu N., Blouin S., Harvey E. J., Smith R. J., Gálvez-Ortiz M. C., Zhang Z. H., 2020, MNRAS, 493, 6001
Lindegren L., 2018, Technical Report GAIA-C3-TN-LU-LL-124-01. Re-normalising the astrometric chi-square in Gaia DR2, Lund Observatory, Lund, Sweden, Available at: http://www.rssd.esa.int/doc_fetch.php?id=3757412
Lindgren S., Heiter U., 2017, A&A, 604, A97
Maldonado J. et al., 2015, A&A, 577, A132
Marsh T. R., 1989, PASP, 101, 1032
McCleery J. et al., 2020, MNRAS, 499, 1890
Miglio A. et al., 2021, A&A, 645, A85
Miller Bertolami M. M., 2016, A&A, 588, A25
Minchev I., Chiappini C., Martig M., 2013, A&A, 558, A9
Minchev I., Famaey B., Combes F., Di Matteo P., Mouhcine M., Wozniak H., 2011, A&A, 527, A147
Nebot Gómez-Morán A. et al., 2011, A&A, 536, A43
Newton E. R., Charbonneau D., Irwin J., Berta-Thompson Z. K., Rojas-Ayala B., Covey K., Lloyd J. P., 2014, AJ, 147, 20
Nissen P. E., Christensen-Dalsgaard J., Mosumgaard J. R., Silva Aguirre V., Spitoni E., Verma K., 2020, A&A, 640, A81
Nomoto K., Kobayashi C., Tominaga N., 2013, ARA&A, 51, 457
Nordström B. et al., 2004, A&A, 418, 989
Pancino E., Carrera R., Rossetti E., Gallart C., 2010, A&A, 511, A56
Parsons S. G. et al., 2012, MNRAS, 426, 1950
Pickles A. J., 1998, PASP, 110, 863
Pilyugin L. S., Edmunds M. G., 1996, A&A, 313, 792
Pinsonneault M. H. et al., 2018, ApJS, 239, 32
Qiu D., Tian H.-J., Wang X.-D., Nie J.-L., von Hippe T., Liu G.-C., Fouesneau M., Rix H.-W., 2020, ApJS, 253, 58
Raskin G. et al., 2011, A&A, 526, A69
Rebassa-Mansergas A., Gänsicke B. T., Rodríguez-Gil P., Schreiber M. R., Koester D., 2007, MNRAS, 382, 1377
Rebassa-Mansergas A., Gänsicke B. T., Schreiber M. R., Koester D., Rodríguez-Gil P., 2010, MNRAS, 402, 620
Rebassa-Mansergas A., Nebot Gómez-Morán A., Schreiber M. R., Girven J., Gänsicke B. T., 2011, MNRAS, 413, 1121

Rebassa-Mansergas A., Ren J. J., Parsons S. G., Gänsicke B. T., Schreiber M. R., García-Berro E., Liu X. W., Koester D., 2016a, MNRAS, 458, 3808
Rebassa-Mansergas A. et al., 2016b, MNRAS, 463, 1137
Renedo I., Althaus L. G., Miller Bertolami M. M., Romero A. D., Córsico A. H., Rohrmann R. D., García-Berro E., 2010, ApJ, 717, 183
Riello M., et al., 2021, Gaia Early Data Release 3. Photometric content and validation, 649, A3
Rocha-Pinto H. J., Maciel W. J., Scalo J., Flynn C., 2000, A&A, 358, 850
Roškar R., Debattista V. P., Quinn T. R., Stinson G. S., Wadsley J., 2008, ApJ, 684, L79
Sellwood J. A., Binney J. J., 2002, MNRAS, 336, 785
Silva Aguirre V. et al., 2018, MNRAS, 475, 5487
Soubiran C., Bienaymé O., Mishenina T. V., Kovtyukh V. V., 2008, A&A, 480, 91
Takeda Y., Ohkubo M., Sato B., Kambe E., Sadakane K., 2005, PASJ, 57, 27
Teixeira G. D. C., Sousa S. G., Tsantaki M., Monteiro M. J. P. F. G., Santos N. C., Israelian G., 2016, A&A, 595, A15
Tody D., 1986, in Crawford D. L., ed., SPIE Conf. Ser. Vol. 627, Instrumentation in astronomy VI. SPIE, Bellingham, p. 733
Torres S., Rebassa-Mansergas A., Camisassa M. E., Raddi R., 2021, MNRAS, 502, 1753
Tremblay P. E., Ludwig H. G., Steffen M., Freytag B., 2013, A&A, 559, A104
Tremblay P. E. et al., 2020, MNRAS, 497, 130
Twarog B. A., 1980, ApJ, 242, 242
Vernet J. et al., 2011, A&A, 536, A105
Willems B., Kolb U., 2004, A&A, 419, 1057
Wojno J. et al., 2018, MNRAS, 477, 5612
Wu Y., Xiang M., Chen Y., Zhao G., Bi S., Li C., Li Y., Huang Y., 2021, MNRAS, 501, 4917
York D. G. et al., 2000, AJ, 120, 1579
Yuan H., Liu X., Xiang M., Huang Y., Chen B., Wu Y., Hou Y., Zhang Y., 2015, ApJ, 799, 135

SUPPORTING INFORMATION

Supplementary data are available at *MNRAS* online.

supl_table.dat

Please note: Oxford University Press is not responsible for the content or functionality of any supporting materials supplied by the authors. Any queries (other than missing material) should be directed to the corresponding author for the article.

This paper has been typeset from a TEX/LATEX file prepared by the author.